Concurrent model for sharp and progressive columnar to equiaxed transitions validated by directional solidification experiments processed in microgravity conditions

Robin Mooney, Laszlo Sturz, Gerhard Zimmermann, Nathalie Mangelinck-Noël, Henri Nguyen-Thi, Yuze Li, David Browne, Shaun Mcfadden

Concurrent model for sharp and progressive columnar to equiaxed transitions validated by directional solidification experiments processed in microgravity conditions

Robin P. Mooney[1,2], Laszlo Sturz[3], Gerhard Zimmermann[3], Nathalie Mangelinck-Noël[4], Henri Nguyen-Thi[4], Yuze Li[4,5], David J. Browne[6], Shaun McFadden[1,7,*]

[1]*Dept. of Mechanical, Manufacturing & Biomedical Engineering, Trinity College Dublin, D2, Ireland*

[2] *(presently at) PM Group, Killakee House, Belgard Square East, D24, Ireland.*

[3]*ACCESS e.V., Intzestrasse 5, 52072 Aachen, Germany.*

[4]*Aix Marseille Univ, Université de Toulon, CNRS, IM2NP, 13397, Marseille, France*

[5] *(presently at) School of Physical Science and Technology, Northwestern Polytechnical University, 710100, Xi'an, China*

[6]*School of Mechanical and Materials Engineering, University College Dublin, Belfield, D4, Ireland*

[7] *(permanent address) School of Computing, Engineering and Intelligent Systems, Magee Campus, Ulster University, BT48 7JL Northern Ireland, United Kingdom.*

**Corresponding author:* s.mcfadden2@ulster.ac.uk

Tel: +44 28 716 75652

Abstract

Columnar and equiaxed structures, which occur during solidification of metallic alloys, influence the texture and properties of castings, welded joints and additively manufactured components. During transient solidification, where grain refiner particles provide the predominant nucleation mechanism, a Columnar to Equiaxed Transition (CET) occurs when conditions that had originally favoured directional columnar growth change to those favouring equiaxed. Constitutional undercooling ahead of the columnar front can permit equiaxed nucleation and growth. By carrying out experiments in microgravity conditions, liquid flows due to thermal and solutal buoyancy effects are suppressed. In these diffusion-controlled conditions, we have observed examples of both sharp (clear) and progressive (gradual) CET. The experimental outcomes, especially the observation of a progressive CET, has highlighted the need for a continuum model that allows for competitive columnar and equiaxed structure development; hence, the Concurrent Columnar to Equiaxed Transition (C2ET) model is proposed. The C2ET is thermally transient and relies on the well-known concept of extended growth for impingement mechanics; thereby, greatly reducing numerical complexity. Importantly, the proposed approach removes the need for a specific equiaxed-blocking criterion, which is often proposed as an essential requirement in other CET models. The C2ET model is validated by four experimental solidification scenarios: two velocity jumps and two thermal-gradient decreases. The velocity jumps induced sharp CETs; whereas, thermal-gradient decreases gave progressive CETs. The C2ET model gave good agreement for the columnar and equiaxed transition zones for both sharp and progressive CET. Results are compared with the classic Hunt model. Unlike Hunt's model, the C2ET model predicted all macrostructure transitions faithfully using a single (or consistent) set of nucleation input parameters across all four scenarios. Since, the same level of grain refinement was used in each experiment, a consistent set of nucleation parameters was expected. The validated approach can enable effective simulation at lower computational cost for industrial processes that rely on a solidification processing step.

Keywords: Solidification; columnar to equiaxed transition; microgravity, nucleation.

1 Introduction

Two forms of grain structure (or textural zones at the macroscale) observed in as-cast alloys are termed columnar and equiaxed. In some cases a columnar to equiaxed transition occurs during solidification, as has been observed in casting, welding, and additive manufacturing processes [1,2]. Columnar structures are sometimes preferred for specific applications as they provide superior creep resistance in alloys that operate at elevated temperatures [3], while fine equiaxed structures are often preferred as they are associated with fewer defects in castings and provide higher yield strengths as described by the Hall-Petch relationship [4,5]. The grain structure can influence post-processing steps such as deformation processing in large ingots. It is shown that steels ingots can be produced with a majority or columnar grains or with a majority of equiaxed grains where equiaxed grains are seen as preferable for any further processing involving plastic deformation [6]. Furthermore, a good test of any model of solidification that aims to treat both columnar and equiaxed cases is its ability to faithfully simulate CET as observed in carefully controlled experiments.

The seminal analytical model of CET was developed by Hunt [7]. The model was developed for steady-state conditions but it is routinely used to predict CET under transient conditions. In Hunt's classic analysis a fully equiaxed morphology was assumed to occur when the volume fraction of equiaxed crystals growing in the undercooled liquid ahead of an array of growing columnar dendrites reached a certain threshold value. This approach has become known as mechanical blocking and is prevalent in CET theory. Since then, alternative theories (such as columnar blocking due to solutal interaction [8]) and advanced computational tools have been developed to track the nucleation and growth of individual grains leading to direct simulation of CET formation. Principal amongst these tools are Cellular Automata (CA) [9], Phase Field (PF) [10], and Front Tracking (FT) [11–13], as summarized in [14]. An approach known as Dendritic Needle Network (DNN) [15] has also been applied to CET [16,17]. These models operate across different length and time scales to cover the corresponding physics – greater physical complexity brings increased computational effort and simulation time. However, computational effort can be reduced by bridging the gap between the simpler analytical model of Hunt and the advanced

computational tools such as CA, PF and FT. An advantage of the bridging-the-gap approach is that CET can be predicted for solidification processes at the industrial scale.

Furthermore, a particular aspect of CET research that has received minor attention is the quantification and characterization of the mixed columnar-equiaxed region between fully columnar and fully equiaxed zones. Microgravity experiments conducted on board the International Space Station [18–21] showed clear evidence of both sharp (with little or no mixed region) and progressive (with a mixed or intermediate region) transitions. The analyses of the progressive transitions included characterization of the aspect ratio of the equiaxed grains that were assumed to nucleate ahead of the columnar front. In the experimental cases exhibiting progressive transitions it was possible to estimate the CET start and finish positions. Hunt [7] did attempt to define the criterion for a mixed columnar-equiaxed region; hence, a more focused review of Hunt's model will be beneficial.

1.1 Hunt Model Overview

In his seminal work on CET, Hunt [7] set out to develop a model that could qualitatively describe the effects of process parameters on CET during steady-state solidification (dendritic front growth rate, temperature gradient, alloy composition, and grain refiner addition). Two approaches were presented: an analytical solution and a numerical model based on integration of the heat flow equation. These models showed good agreement and, therefore, the simpler analytical model has become one of the most frequently used methods to describe the conditions for fully-equiaxed structures. Hunt's criterion is as follows

$$G < 0.617 N_o^{1/3} \left(1 - \frac{\Delta T_N^3}{\Delta T_c^3}\right) \Delta T_c. \quad (1)$$

For a solidification front growing with a columnar tip undercooling, ΔT_c, the model predicts a transition to fully-equiaxed morphology when the temperature gradient, G, satisfies the inequality in equation (1). The equiaxed nucleation conditions are described by the seed density, N_o, and the nucleation undercooling, ΔT_N. Hunt assumed that the nucleation conditions quickly reached saturation point so that nucleation could be described by a single value of undercooling, ΔT_N. The expression in equation (1) is derived based on a mechanical blocking criterion as follows: when the crystals' aspect ratios are greater than two, they may be considered more columnar than equiaxed. This threshold of two on aspect ratio leads to an

extended volume fraction criterion of $\phi_E > 0.66$, which, in turn, leads to a blocking fraction of $\phi > 0.49$ as the criterion for a fully-equiaxed morphology.

Similarly, Hunt decided on an extended volume fraction criterion of $\phi_E < 0.0066$ for a fully columnar structure; hence, the following inequality was provided for a fully columnar structure [7]:

$$G > 0.617(100N_o)^{1/3}\left(1 - \frac{\Delta T_N^3}{\Delta T_c^3}\right)\Delta T_c. \quad (2)$$

The inequalities given in equations (1) and (2) demark the conditions for fully equiaxed and fully columnar structures. According to the model, the subset of temperature gradients between these inequalities defines the operating window where mixed columnar-equiaxed structures should prevail.

Hunt admitted that the selection of the blocking fraction criterion of $\phi > 0.49$ for fully equiaxed was rather arbitrary; even though, in so doing, it provided the earliest example of a definition of an equiaxed crystal (i.e., with an aspect ratio of less than two). If the selection of the fully equiaxed criterion was described as arbitrary, then perhaps the definition of a fully columnar structure was even more so. The criterion for the fully-columnar structure was simply obtained by reducing the equiaxed extended volume fraction by two orders of magnitude to give 0.0066. The evaluation of the criterion for fully columnar structures (i.e., $\phi_E < 0.0066$) has received little or no serious critical review. For example, in other seminal work by Gäumann et al.[22], improvements to nucleation kinetics were added to the framework of Hunt by taking into account the liquidus temperature profile in the constitutionally undercooled liquid ahead of the columnar front and KGT growth kinetics [23] for the columnar front. However, to simplify the comparisons, Gäumann et al. used a unique blocking fraction of $\phi = 0.5$ as the CET criterion. Effectively, the criterion for the transition of fully columnar to an intermediate columnar-equiaxed structure (i.e. equation (2) using $\phi_E < 0.0066$) was ignored.

1.2 Blocking criteria with application to CET modelling

Within literature, two main criteria for predicting fully equiaxed macrostructure have been developed: mechanical blocking based on the Hunt analysis and solutal blocking based on solutal interactions between equiaxed dendrites and the columnar front [8].

Flood and Hunt [24] proposed one of the earliest model of CET that used the mechanical blocking criterion. They used a model of columnar solidification [25] and incorporated a model of equiaxed solidification based on the classic Avrami equation ahead of the columnar front. They used the criterion of $\phi = 0.49$ as the equiaxed blocking fraction.

Since Flood and Hunt, several authors have critically reviewed the selection of the blocking fraction and alternative values have been proposed. Biscuola and Martorano [26] proposed a blocking fraction as low as $\phi = 0.2$ or Al-7wt.%Si, Sachi et al. [27] used a blocking fraction of $\phi = 0.5$, Pineda and Martorano [28] found improved agreement in their results with a blocking fraction of $\phi = 0.99$ and Mirihanage et al. [29] proposed a blocking fraction of unity with their macroscopic model of CET. The range of blocking fractions proposed in the literature (from 0.2 to unity) demonstrates the importance of model validation with experimental datasets in order to characterize any given model's blocking fraction when using the mechanical blocking criterion. The blocking fraction is seen as highly dependent on the scenario and should therefore be assumed as case-specific and subject to validation.

Martorano et al. [8] proposed a blocking criterion based on the presence of elevated solute levels in the extra dendritic liquid between equiaxed crystals. The elevated solute levels were assumed to cause interaction (that is, growth restriction leading to growth arrest) between the columnar front and the equiaxed grains. This application of this mechanism for CET replaced the need for a mechanical blocking fraction and has become known as solutal blocking.

Wu and Ludwig [30] presented the three-phase region model for mixed columnar and equiaxed solidification. This model has the capacity to model columnar and equiaxed fractions of the same phase simultaneously. This model incorporated the facility for a soft blocking mechanism that can lead to solutal blocking or it can use the hard or mechanical blocking criterion, as required. The model was developed to incorporate melt convection and grain sedimentation. A 1D model of a directional solidification case was investigated and the question of which blocking mechanism was addressed. It was recommended that both solutal and mechanical blocking mechanisms should be considered and for the 1D case analyzed, the mechanical blocking mechanism of Hunt was found to be most relevant in specific cases. Further extensions to this model to five phase regions has been developed [31] and a parametric study was applied to investigate CET [32]. As with earlier work, columnar and equiaxed phases were modelled concurrently and, in the 1D case, the model showed evidence of solutal interaction but ultimately the Hunt criterion was seen as relevant for predicting

CET. In a 3D cylindrical scenario, grain sedimentation was expected to play a role in the morphology prediction. This was highlighted in ref. [32] as an area for further work. The work of Wu et al. is reviewed in ref [33].

Wołczyński et al. [34] provided experimental evidence of CET during solidification of Brass ingots. They showed chill, columnar (fine and coarse), equiaxed and single crystal (axial) zones. Areas of transition were observed where the features from two zones were evident, such as coexisting columnar and equiaxed crystals. They produced a mathematical model and reviewed the temperature gradient and liquidus isotherm velocity versus time. Their model predicted that thermal gradients became constant when CET occurred. This was likely due to the latent heat from the equiaxed nucleation and growth ahead of the columnar front. The Wołczyński et al. [34] model showed a transition from fully columnar to fully equiaxed conditions by allowing the columnar growth velocity tend to zero over the transition zone while, simultaneously, allowing the equiaxed front velocity increase from zero to match the solidification front velocity by the end of the transition. During their model's simulated transition, columnar and equiaxed grains are assumed to co-exist.

The CET as typically described in literature is observed in the final microstructure, that is, through post-mortem or ex-situ microstructural analysis. In-situ investigation by X-ray radiography offers the significant advantage of observing the microstructure during its formation. Ngomesse et al. [35] observed CET occurring in directionally solidified Al-20wt.%Cu alloy with 0.1 wt.% Al-Ti-B grain refiner added. Experiments were conducted in microgravity (onboard the MASER-14 sounding rocket) and in terrestrial gravity with three orientations relative to gravity: horizontal, vertical upwards, and vertical downwards. The impingement of equiaxed grains with the columnar mush was classified as either mechanical (hard) blocking, i.e., showing direct contact of dendrite tips, or solutal (soft) blocking, i.e., growth arrest due to the accumulation of solute around dendrite tips prior to direct contact. Solutal and mechanical blocking was observed; however, mechanical impingement was seen to be predominant over solutal impingement in all cases. For the microgravity and horizontally aligned terrestrial cases, mechanical impingement events strongly outnumbered solutal blocking events: 10 to 1 for microgravity and 19 to zero for horizontal. Upward and downward solidification cases were more balanced but still had higher numbers of mechanical impingement events to solutal impingements: 9 to 6 for upward and 12 to 4 for

downward. Flow caused by the solidification shrinkage was seen to play a key role in the impingement mechanisms and the final microstructure.

Given the clear evidence of sharp and progressive CETs from microgravity experiments (which were free of sedimentation effects), a model is required that treats the columnar to equiaxed transition as a progressive phenomenon. Given the lack of a consistent mechanical blocking fraction across several modelling approaches and the argument of solutal versus mechanical blocking, a model that is independent of a blocking criterion would be advantageous. Hence, the current paper reports on a new computationally-efficient, targeted-physics model that has been validated against the reported experimental findings conducted in microgravity [19–21,36]. One of the aims of the modelling approach is to investigate the level of physics that is commensurate to modelling the problem at hand at the macro scale of the process in order to give reliable results with low computational complexity. The model allows for fully columnar, fully equiaxed, and a transient zone in between (similar to the work of Wu and co-workers). A distinct difference with the proposed model is that the simple blocking criterion, such as that proposed by Hunt [7], is not required. The model simulates a gradual evolution from columnar to equiaxed over a spatial range that is dependent on the conditions rather than predicting a sharp transition point defined by a threshold value. This model is called the Concurrent Columnar Equiaxed Transition (C2ET) model and it focuses attention on the often-overlooked topic of progressive CET.

1.3 Aim and objectives

An aim of this manuscript is to present the Concurrent Columnar Equiaxed Transition (C2ET) model, developed to predict results from microgravity solidification experiments that displayed both sharp and progressive columnar to equiaxed transitions. A clear objective of the C2ET model is to provide an alternative, targeted physics, approach to modelling CET that does not require a specific blocking fraction criterion but instead allows columnar and equiaxed grains to nucleate and grow concurrently and competitively. The intention is to demonstrate the effectiveness of the proposed C2ET model in predicting an intermediate region that transitions from fully columnar to fully equiaxed. Hence, a distinct advantage of the C2ET approach is that it is capable of modelling the fractions of the competing columnar

and equiaxed morphologies during solidification and in the final macrostructure. The following objectives are provided in order to fulfil the stated aim:

1. Develop and describe the details of the newly proposed C2ET model.
2. Apply the C2ET model in order to match the thermal conditions from the microgravity CET experiments.
3. Compare, on a case-by-case basis, the simulated predictions for columnar and equiaxed morphologies to those observed during microgravity conditions.
4. Critically evaluate the outcomes of C2ET model to Hunt's [7] mechanical blocking criterion and the process-structure relationship.

Section 2 of this manuscript, Materials and experimental methods, summarises the experimental processing details for the microgravity experiments that were performed on board the ISS. Section 3 is then expanded to provide a detailed account of the C2ET modelling approach. Section 4, Results, provides thermal and microstructural evaluations from both experimental and simulated approaches for comparison purposes. The Discussion, section 5, provides a critical evaluation on the agreement between the C2ET predictions and the experimental findings and then goes on to critically evaluate the C2ET results against representative outputs from the mechanical blocking approach.

2 Materials and experimental methods

Microgravity solidification experiments on CET in grain refined Al-7wt.%Si were performed on board the International Space Station. Detailed accounts of the experimental apparatus and findings have been provided elsewhere [18–21]. Nevertheless, the relevant experimental details are summarised in the following sections.

2.1 Furnace details and experimental process parameters

Sample materials were delivered to the ISS on two separate missions as part of the CETSOL project [37]. The first batch of Sample Cartridge Assemblies (SCA) were processed using the Low Gradient Furnace (LGF) facility [18]. The second batch of SCA were processed on the Solidification and Quenching Furnace (SQF) [19–21].

The SCAs contained cylindrical samples of Al-7wt.%Si alloy (grain refined with additions of Al-Ti-B) with nominal diameter of 7.8 mm and length, 245 mm. Each sample was contained

within Al_2O_3 cylindrical crucibles. The coaxial furnace elements were translated in a controlled way along the length of the SCA. By controlling the temperatures and the translation speed of the furnace elements, directional solidification was achieved. Temperature gradient, cooling rate, translation speed and translation distances were controlled to give conditions suitable for CET.

Of the SCAs processed, those of interest in this study are summarised in Table 1 along with their processing parameters during the different cooling stages. Two distinct approaches were used to trigger CET: (1) Velocity Jump (VJ) and (2) Gradient Decrease (GD). The velocity jump procedure involved an initial cooling stage (stage I) with constant temperature gradient but with relatively low translation speed followed an abrupt step-up change to a cooling stage with higher translation speed and increased cooling rate (stage II). The gradient decrease procedure involved a constant translation speed across cooling stages I and II. Stage I had constant temperatures and temperatures gradients across the furnace elements. Stage II included the application of a cooling rate to the furnace elements of the hot zone to induce a decreasing temperature gradient within the sample. Stage II in all cases was followed by stage III, a rapid quenching phase, to complete the process. Thermocouples were placed uniformly along the length of the crucible to measure the thermal responses of each scenario.

Table 1: Furnace process parameters for the four scenarios of interest. (VJ refers to Velocity Jump whereas GD refers to Gradient Decrease; FM refers to Flight Module.)

Scenario Name	VJ#1	VJ#2	GD#1	GD#2
Alloy	Al-7wt.%Si + grain refiners (0.5 wt.% of master alloy AlTi5B)			
Flight Batch	1	2	1	2
Sample Cartridge Assembly	FM1	FM1	FM5	FM7
Preparatory Stage:				
Initial Gradient, G_i (K mm^{-1})	0.9	4.0	0.9	3.0
Homogenisation Time, t_i (s)	600	14400	600	3600
Stage I:				
Translation Speed, V_I (mm s^{-1})	0.01	0.02	0.01	0.02
Translation Distance, S_I (mm)	20	20	20	30
Stage II:				
Translation Speed, V_{II} (mm s^{-1})	0.20	0.20	0.01	0.02
Cooling Rate, $\dot{T}_{II}$ (K s^{-1})	0.067	0.133	0.067	0.133
Translation Distance, S_{II} (mm)	50	50	20	50
Stage III:				
Translation Speed, V_{III} (mm s^{-1})	3	Rapid Quench	3	Rapid Quench

2.2 Experimental methods and overview of previous findings

When samples were returned to earth, they were prepared for microscopic examination. Dendritic structures were revealed by electrolytic etching and polarised optical microscopy. Electron Backscattered Diffraction (EBSD) was used selectively to analyse the grain structure based on crystallographic orientation. In particular, samples were assessed for the presence and location of CET. Detailed results for VJ#1, VJ#2, and GD#1 are provided elsewhere [18–20]. Results for GD#2 are being published for the first time.

Table 2 provides a summary of the macrostructural analysis that is relevant to the current

work. The velocity jump experiments (VJ#1 and VJ#2) showed a sharp transition from columnar to equiaxed at the reported locations given as $x_{CET,min}$. The gradient decrease experiments showed progressive transitions from columnar to equiaxed over a distance in the sample. The extents of the transition ranges for GD#1 were observed and recorded as $x_{CET,min}$ (defined at the position at which the columnar grains that started their growth in stage I where stopped) and $x_{CET,max}$ (defined as the position at which equiaxed grains are no longer considered as elongated, i.e., an elongation factor lower than two). Within this range the sample transitioned with a progressive CET that became more equiaxed closer to the position $x_{CET,max}$. For sample GD#2, the extents of the CET were difficult to establish, the microstructure showed an incomplete CET transition with columnar dendrites in the initial section but with an increase in presence of equiaxed dendrites leading up to the final section. Nevertheless elongated (columnar) isolated dendrites were clearly observed throughout the length of the sample, but with reduced occurrence along the length of the processed sample (see Figure 11). Experimental details are presented in the Results section of this manuscript for all cases.

Table 2: Information regarding the nature of the CET found in each scenario (the CET type and a brief description and location information).

VJ#1	VJ#2	GD#1	GD#2
CET Type: Sharp	CET Type: Sharp	CET Type: Progressive	CET Type: Progressive
Description: A CET at a well-defined location: $x_{CET,min} = 127mm$	Description: A CET at a well-defined location: $x_{CET,min} = 134mm$	Description: A progressive CET with elongated grains between two locations: $x_{CET,min} = 130mm$ $x_{CET,max} = 156mm$	Description: Progressive transition from columnar to majority equiaxed over the range $147mm$ to $237mm$.

3 Model development

3.1 Thermal model

For modelling purposes, the region of interest on the SCA was the sample itself and the Al_2O_3 crucible which had thermocouples embedded within. Hence, the modelling domain consists of two coaxial components. Figure 1 shows how the two interacting thermal models were coupled.

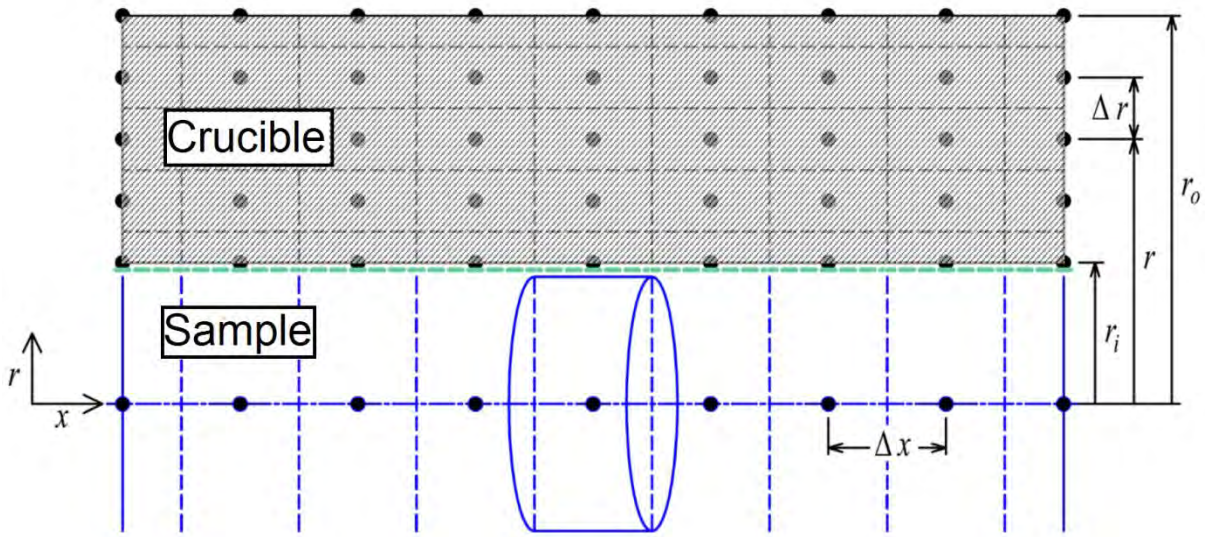

Figure 1: Control volume meshing details for the thermal finite difference model. The sample was modelled with 1D axisymmetric geometry. The crucible was modelled with 2D axisymmetric geometry. (Image for demonstration only and is not to scale)

The crucible was modelled with a 2D axisymmetric heat equation with radial and axial coordinates, *r* and *x*, respectively:

$$\frac{\partial(\rho c_p T)}{\partial t} = \frac{1}{r}\frac{\partial}{\partial r}\left(rk\frac{\partial T}{\partial r}\right) + \frac{\partial}{\partial x}\left(k\frac{\partial T}{\partial x}\right) \quad (3)$$

The discretisation scheme used was an Eulerian method similar to that used in Battaglioli et al. [38] but without the need for latent heat or advection terms. The thermal conditions were mainly imposed by the relative motion between the moving furnace elements and the stationary sample; hence, it was appropriate to use a fixed-grid mesh but with time-dependent boundary conditions. The measured temperature data from the thermocouples were

interpolated with reference to their time and space coordinates and applied to the external surface of the crucible as a boundary condition. This arrangement was fully representative of the experimental procedure.

For assembly purposes, the sample needed to slide into the crucible and therefore had to be a sliding fit; hence, the nominal internal diameter on the crucible was $r_i = 8$ mm and the nominal diameter of the sample was 7.8 mm. The resulting gap between the crucible and the sample would have created an additional thermal resistance, R_{gap}, which was included into the model between the crucible and the sample at their interface:

$$R_{gap} = \frac{1}{h_I}. \tag{4}$$

Here, h_I represents an interfacial heat transfer coefficient.

The sample was modelled using 1D cylindrical geometry via the heat equation

$$\frac{\partial(\rho c_p T)}{\partial t} = \frac{\partial}{\partial x}\left(K\frac{\partial T}{\partial x}\right) - \frac{2}{r}h_I(T - T_I) + \rho L g_s \frac{\partial \zeta_V}{\partial t} + \rho L \zeta_V \frac{\partial g_s}{\partial t} \tag{5}$$

The term on the left of the equation is the rate of change of sensible heat where ρ is density and c_p is specific heat capacity. The terms on the right are the conduction term for axial heat flow (with temperature and phase dependent thermal conductivity, K); the surrounding term for the radial heat flow (with temperature on the crucible interface, T_I); the latent heat term due to the volumetric evolution of the mushy zone (latent heat, L; volume fraction of mush, ζ_V; and local solid fraction within the mush, g_s); and the latent heat term associated with thickening of the mushy zone, respectively. Overall solid fraction is obtained as the product of local solid fraction within the mush by the volume fraction of mush and is given as $g_s\zeta_V$. This equation is based on the Bridgman Furnace Front Tracking Model (BFFTM) of Mooney et al. [39] but with no requirement to include an advection term similar to the application of the BFFTM reported in [40]. The formulation of the heat equation (eq. (5)) is valid for cases where the radial temperature gradient in the sample is sufficiently low compared to the axial temperature gradient so that the temperature can be assumed constant in the radial direction. The Biot number is determined as

$$Bi = \frac{h_I L_C}{K} \tag{6}$$

The characteristic length is L_C which is the control volume divided by its circumferential area giving $L_C = r_i/2$. This 1D approach is valid when the Biot number is less than 0.1 ($Bi \leq 0.1$) [39]. The local solid fraction within the mushy zone is calculated based on the Scheil equation and the eutectic transformation is assumed to take place isothermally at the eutectic transformation temperature. Detailed accounts of the solid fraction algorithm used are provided elsewhere [12].

3.2 Columnar model

The BFFTM uses a marker to designate the position of the columnar dendrite tips, that is, the marker denotes the extent of the columnar zone (as shown in Figure 2). The marker is initially placed on the left boundary and moves after a pre-defined nucleation undercooling is reached. Once nucleated, the marker is constrained to move along the axis of the sample, but is free to move to any point between the control volume nodes (generally, the marker moves from left to right). The magnitude of the marker motion, v_t, is determined by the steady-state growth rate law

$$v_t = C\Delta T^b \tag{7}$$

where ΔT is the tip undercooling relative to the equilibrium liquidus temperature ($\Delta T = T_L - T$), C is the growth constant, and b the growth exponent. Other models (e.g., [8]) account for the effect of local solute enrichment in supressing the liquidus temperature and, hence, reduction in columnar growth rate in the final stages of solidification. Since the current model uses equilibrium liquidus throughout, it relies on the principle of extended growth (or the JMAK approach) to capture the impingement mechanics. This aspect is discussed later in this section.

When a marker passes through a control volume, the position of the marker relative to the encroached control volume boundary is required to determine the volume captured by the columnar growth, V_{col}, where

$$V_{col} = dA. \tag{8}$$

Here d is the distance encroached by the marker into the control volume and A is the cross section area of the sample. When a marker has passed through and has captured fully the control volume then $V_{col} = V_{CV}$ (where V_{CV} is the control volume size).

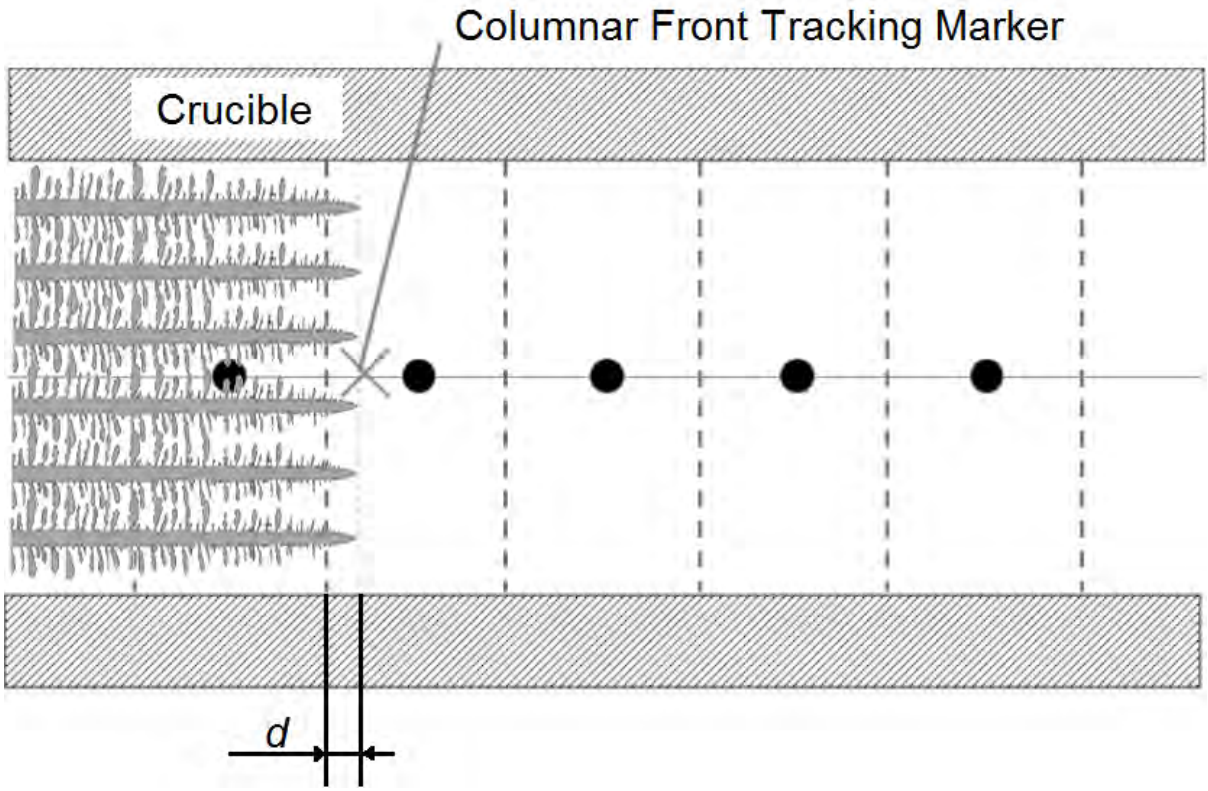

Figure 2: Illustration of the columnar front tracking method for the 1D axial case. Dashed lines represent the interfaces between control volumes, circles (•) represent control volume node centres, and the marker (×) represents the position of the columnar front.

The BFFTM model, which has been adapted in this study, has been subjected to scrutiny and verified against an analytical Naumann model [41]. It has been applied to stationary Bridgman [40] and transient Bridgman solidification conditions [42].

3.3 Equiaxed model

Polycrystalline equiaxed nucleation and growth was modelled using the Nucleation Progenitor Function (NPF) approach [43]. This approach requires an athermal description of nucleation undercooling known as progenitor function (modelled with a Gaussian distribution).

$$\frac{dN}{d(\Delta T)} = \frac{N_o}{\Delta T_\sigma \sqrt{2\pi}} exp\left[-\frac{1}{2}\left(\frac{\Delta T - \Delta T_\mu}{\Delta T_\sigma}\right)^2\right] \quad , \tag{9}$$

where N_o is the volumetric nucleation (seed) density, ΔT_μ is the average nucleation undercooling, and ΔT_σ is the nucleation standard deviation. The NPF determines the actual

nucleation rates within each control volume which are then called progeny functions. By simulating the so-called progenitor-progeny relationships, the NPF model estimates the extended equiaxed volume as

$$V_{equ,EX} = \frac{4\pi}{3} V_{CV} \int_0^t \dot{N}(t_n) \left[\int_{t_n}^t v_t dt' \right]^3 dt_n \tag{10}$$

$\dot{N}$ is the volumetric equiaxed nucleation rate; t is the current time variable; t_n, and t' are also time variables associated with the integration process. Variable t_n is associated with nucleation time and t' is an intermediate time-based, integration variable. All of the terms in equation (10) have the same meaning as provided in ref. [43]. The concept of extended volume, which was developed by Kolmogorov [44], is important to understanding the JMAK or Avrami equation [45,46] and the NPF model. Extended volume is obtained by considering the sum total of all real and phantom growth [47]. Phantom growth is the key concept in the derivation of the JMAK equation – it is growth that occurs within previously transformed regions (called overgrowth) that is unphysical but yet, when accounted for mathematically, gives the extended volume. Extended volume fraction is then transformed to volume fraction through application of the JMAK equation, which accounts for impingement. If local solute enrichment were applied to the undercooling in the growth equation, (equation (7)) then the undercooling would diminish and growth would arrest before extended volume due to overlapping volumes could develop. Although, experiments show solutal interaction and growth arrest at impingement [48], the current model relies on the conceptual approach of extended volume (growth overlap and phantom nucleation) to give a representation of mechanical impingement – similar to the JMAK framework. Solutal or soft impingement can be considered in the JMAK framework; but, given the experimental findings of Ngomesse et al. [35], mechanical impingement events were shown to strongly outnumber solutal blocking events in the microgravity scenario.

3.4 Concurrent Columnar to Equiaxed Transition Model

The fundamental hypothesis or basis for the C2ET model is that columnar or elongated growth and equiaxed growth should be allowed to grow concurrently and competitively. Figure 3 shows a representative view of the C2ET at the macroscale. Generally, columnar growth (as represented by the columnar marker) nucleates and grows in the solidification direction. The marker is at some finite temperature below the liquidus temperature; hence,

undercooled liquid can exist ahead of the marker. This undercooled liquid provides the opportunity for equiaxed nucleation and growth ahead of the columnar marker. So, both columnar mush and equiaxed mush can coexist within the same control volume. If neither mushy volume can mathematically block the other, then phantom growth will be generated between the two dendritic morphologies as they grow over each other. Figure 4 shows a particular case where a control volume contains both columnar and equiaxed growth volumes; but, the columnar region contains phantom equiaxed growth.

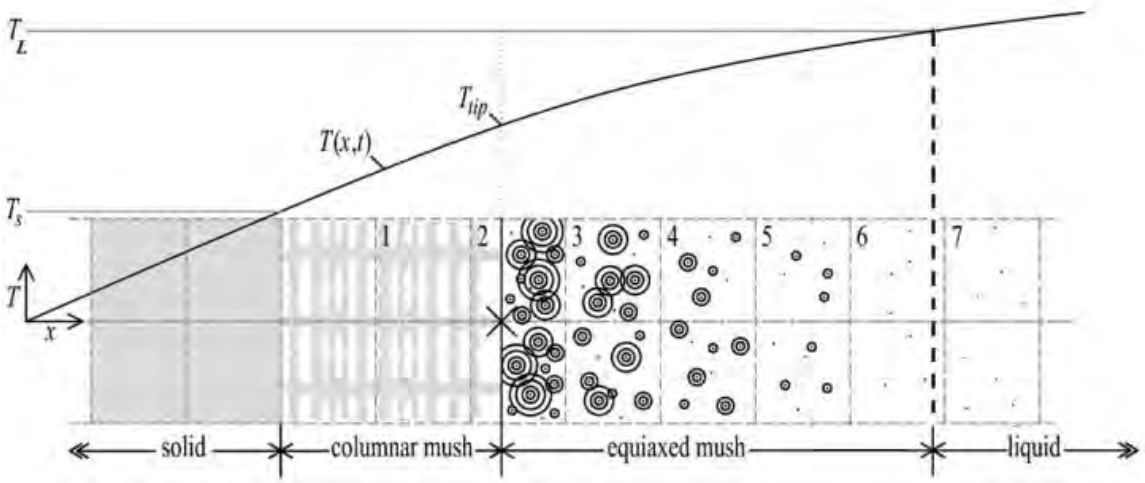

Figure 3: Illustration of the concurrent C2ET modelling approach which allows columnar and equiaxed mushy regions to nucleate and grow simultaneously.

Extended growth within the control volume must consider the sum total of the captured columnar growth and the extended equiaxed growth volume, so that the extended volume fraction is given by

$$\zeta_{EX} = \frac{V_{col} + V_{equ,EX}}{V_{CV}} \tag{11}$$

The overall volume fraction of mush at any control volume is then calculated using the classic Avrami equation:

$$\zeta_V = 1 - exp(-\zeta_{EX}) \tag{12}$$

This is the volume fraction that is used in equation (5) for the latent heat terms.

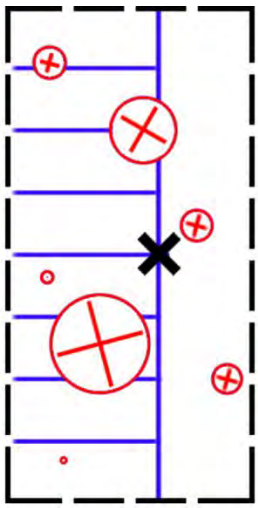

Figure 4: Detailed illustration of a control volume that contains both columnar mush (striped area left of marker ×) and equiaxed mush (circular crosshairs, ⊗). Note how an individual equiaxed crystal can exist as phantom growth within the columnar mush or as real growth in the liquid region to the right of the marker.

The final consideration in the C2ET model is to distinguish the volume fractions of columnar and equiaxed within any control volume. The real volume fraction of columnar growth is taken as

$$\zeta_{col} = \frac{V_{col}\left(1 - \zeta_{equ,A}\right)}{V_{CV}} \tag{13}$$

Where $\zeta_{equ,A}$ is the estimated equiaxed fraction without consideration for (in the absence of) columnar growth and is calculated via

$$\zeta_{equ,A} = 1 - exp\left(-\frac{V_{equ,EX}}{V_{CV}}\right) \tag{14}$$

Since the equiaxed morphology does not exist in isolation, it exists within the columnar region and in the liquid region ahead of the columnar tips, the real equiaxed fraction is considered to be

$$\zeta_{equ} = \zeta_V - \zeta_{col} \tag{15}$$

The concurrent calculations for the columnar and equiaxed fractions are allowed to continue until the control volume is fully captured by the growth.

3.5 Thermophysical properties and modelling parameters

The thermophysical data used for the Al-7wt.%Si alloy were taken from [49] which provides a collection of data from various experimental sources. The nucleation parameters for the NPF model were taken from Liu et al. [36] who used a CAFE model to simulate the experiments. Hence, assuming a normal distribution, the overall condition of the inoculant particles is described by three statistical parameters, $N_o = 5 \times 10^{10}$ m^{-3}, ΔT_μ = 4 ºC, and ΔT_σ = 0.5 ºC. The spatial discretisation used was Δx = 0.5 mm and Δr = 0.712 mm. The time resolution used was Δt = 0.001 seconds. The interfacial heat transfer coefficient was estimated as $h_I = 1000$ W/(m^2·K).

4 Results

Figure 5 compares the thermal time data from the experiments to the outputs from the simulations. The four separate plots, Figure 5(a) to (d), represent each scenario summarised in Table 1. Solid lines represent the measured thermocouple data while dashed lines represent the output from the simulation at the same locations.

Figure 6 shows a montage of time-series plots from the simulation of GD#1. This style of plot is known as an area plot, where the data for the different volume fractions are stacked upon each other. The sum total of all volume fractions equals unity; hence, the axis scaling ensures that coloured areas between the curves represent the relevant volume fractions along the length at all times. Figure 6 also shows g_s, which is local solid fraction within the mush envelopes. The solid fraction calculation follows a Scheil-based formulation; hence, the eutectic transformation is represented by the step change in the g_s curve. It should be noted that the overall solid fraction at any location is obtained by multiplying local solid fraction within the mush by the volume fraction of mush, that is, solid fraction is given as the product $g_s\zeta_V$. Hence, even though figure 6 shows $g_s > 0$ in advance of the columnar zone, the volume fraction of mush, ζ_V, is low and therefore overall solid fraction is also much lower than g_s.

The plot Figure 6(f) shows the prediction for the fully solidified sample, where the area plot shows the proportion of columnar and equiaxed fractions in the final macrostructure. The progressive nature of the CET prediction from the C2ET model is clearly shown over the

mid-range of the sample length. Note that an unmelted region is shown on the left-hand side. The unmelted region was present on each sample processed. Figure 6 shows scenario GD#1 as a representative output from the model. Similar results for all scenarios have been recorded as animated video sequences and are available online as supplementary material.

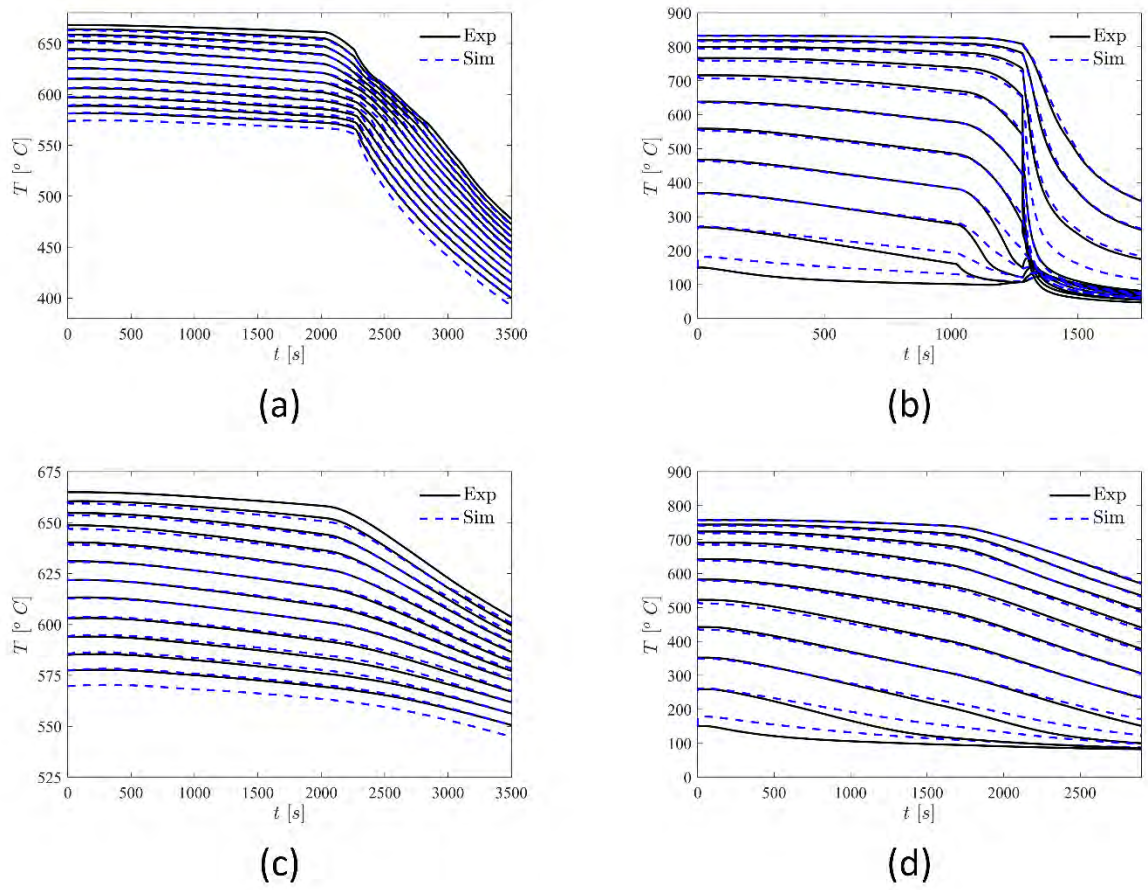

Figure 5: Temperature histories (experimental versus simulated) at the thermocouple positions for each scenario: (a) VJ#1, (b) VJ#2, (c) GD#1, and (d) GD#2.

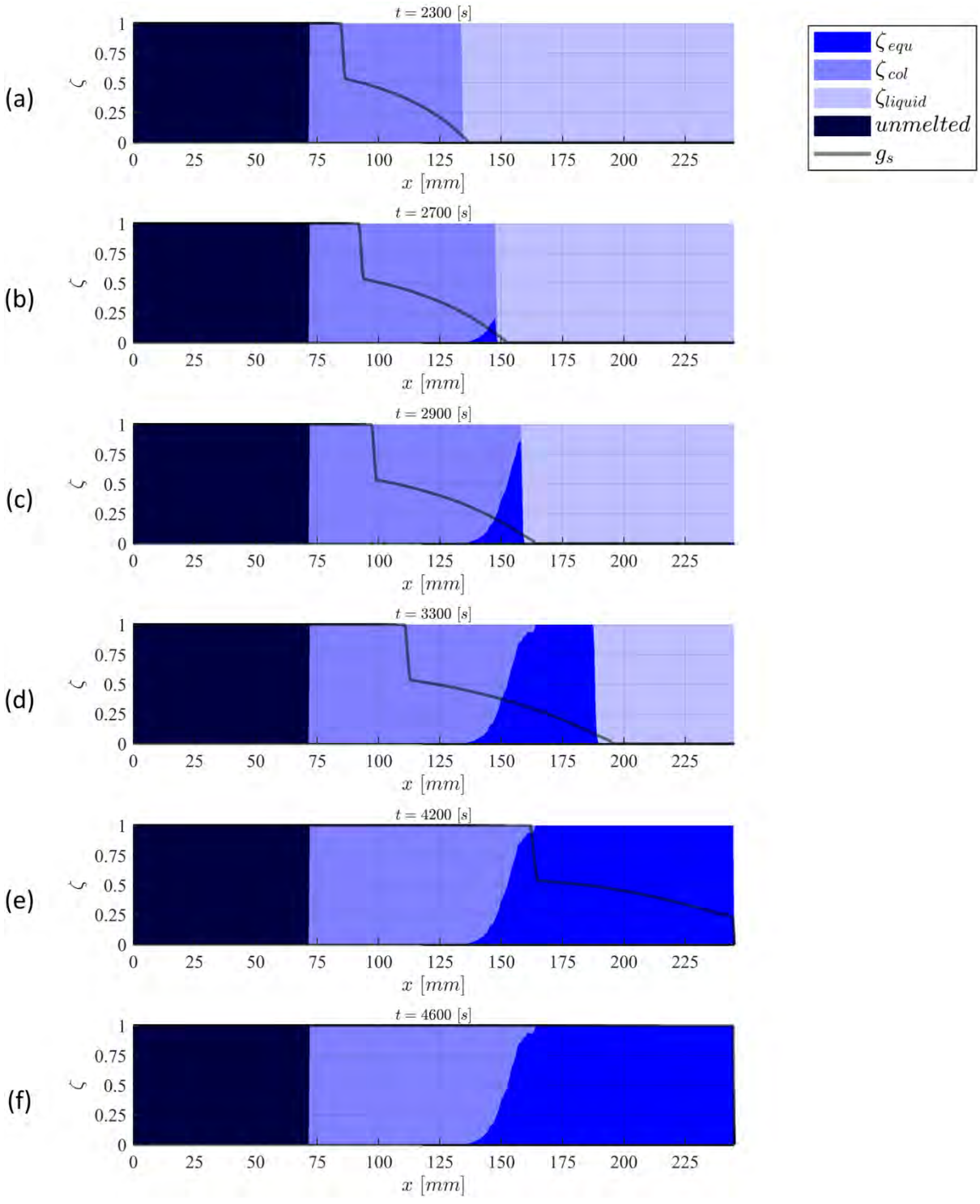

Figure 6: Sequence of plots showing the transient evolution of mush in the axial direction for scenario GD#1. The dark region to the left represents the unmelted solid; ζ_{col} is columnar mush; ζ_{equ}, equiaxed; and ζ_{liquid}, liquid. Solid fraction within the mush, g_s, is shown as a solid line plot. Times: (a) 2300 s, (b) 2700 s,(c) 2900 s, (d) 3300 s, (e) 4200 s, (f) 4600 s.

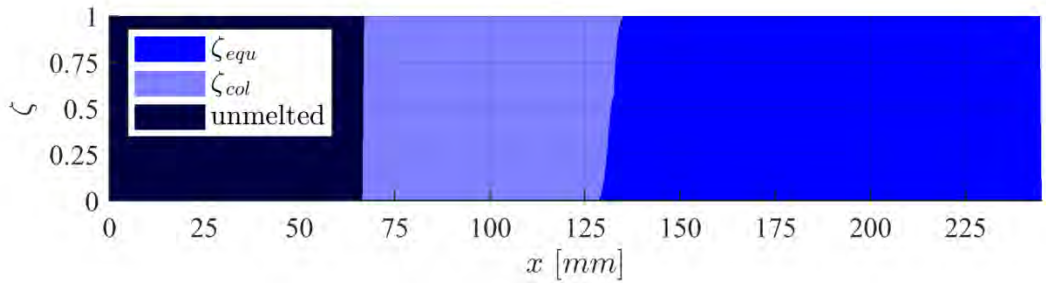

Video 1: Animation link (clickable) for VJ#1

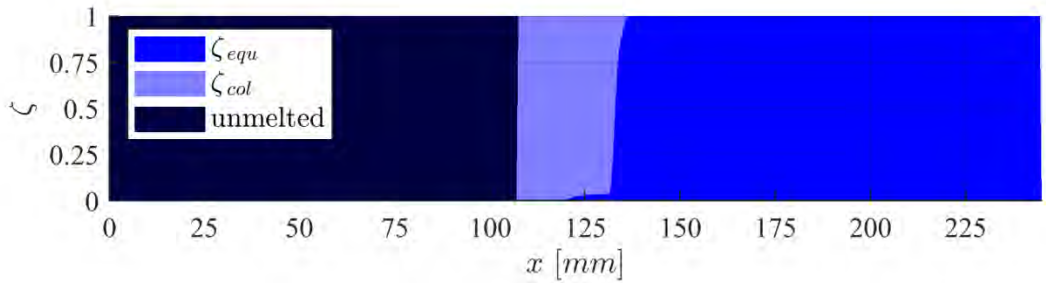

Video 2: Animation link (clickable) for VJ#2

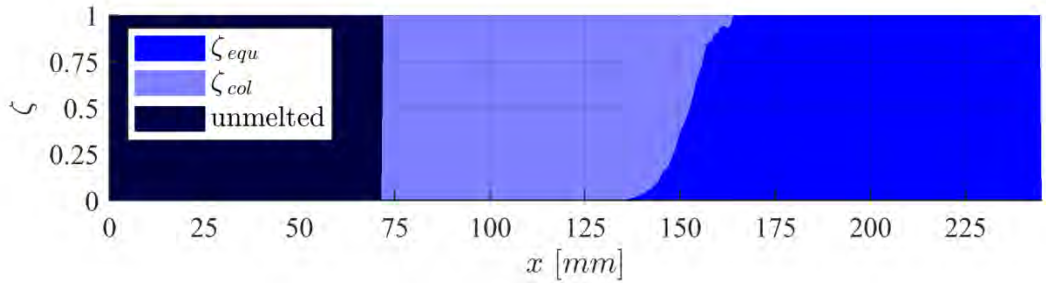

Video 3: Animation link (clickable) for GD#1

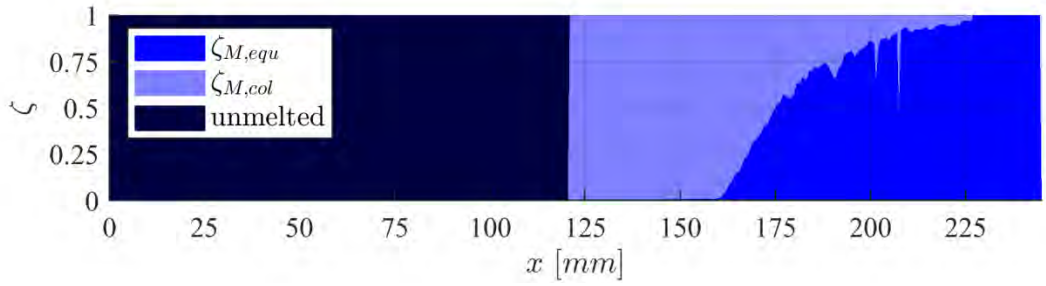

Video 4: Animation link (clickable) for GD#2

Figure 7 to 10 show the final simulated predictions for the columnar and equiaxed volume fractions for all four scenarios simulated: VJ#1, VJ#2, GD#1, and GD#2. Additionally, the representative portions of the microstructure analysis for each experimental case are provided for reference. The dotted (yellow) lines show where the extents of each micrograph correspond to the positions on the horizontal axes. The vertical dashed lines (in red) show where the coordinates of the measured CET positions correspond to the horizontal axes. Figure 8 presents an EBSD colour map in addition to the micrograph. Every grain on the EBSD plot is assigned a colour based on its crystallographic orientation.

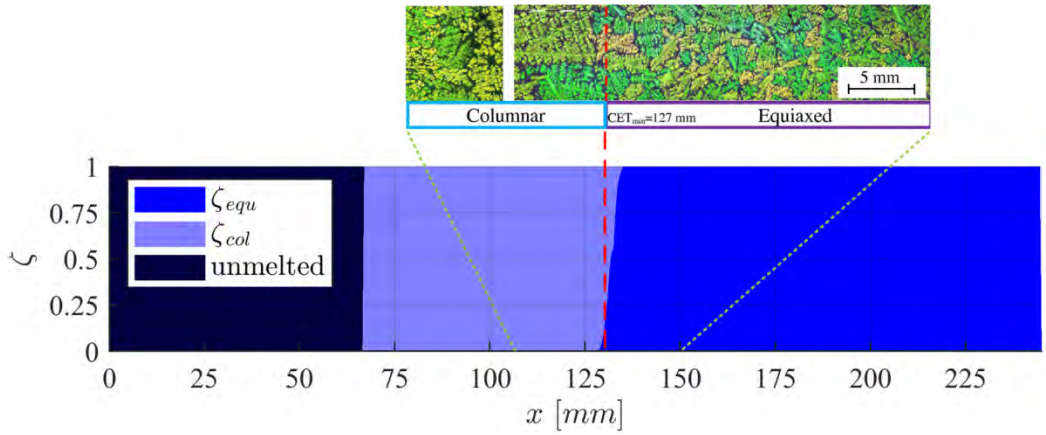

Figure 7: Final plot from the simulation for scenario VJ#1 showing the volume fractions, ζ, for unmelted, columnar and equiaxed regions. Optical macrograph image is shown to scale for comparison.

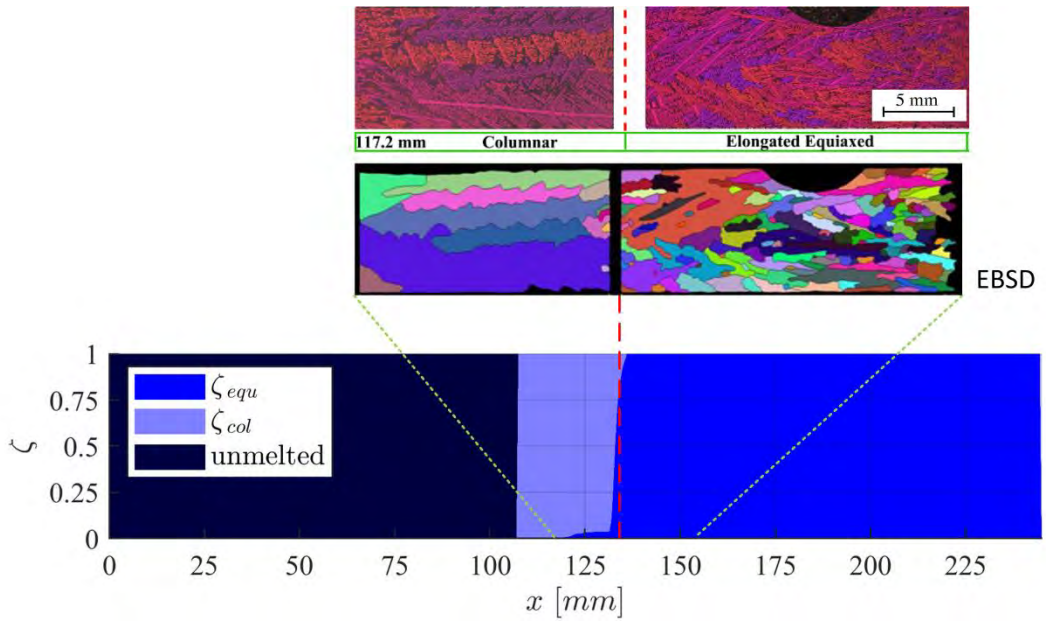

Figure 8: Final plot from the simulation for scenario VJ#2 showing the volume fractions, ζ, for unmelted, columnar and equiaxed regions. Optical macrograph and Electron Back Scattered Diffraction images are shown to scale for comparison.

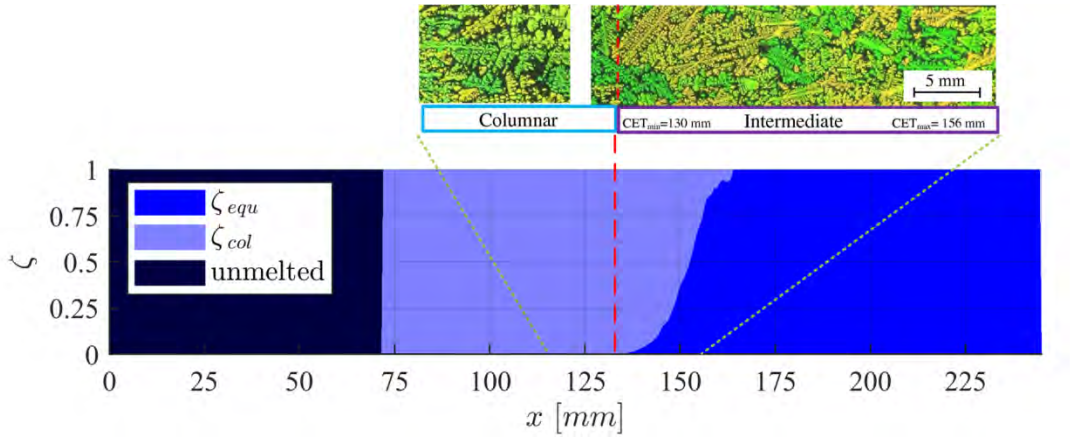

Figure 9: Final plot from the simulation for scenario GD#1 showing the volume fractions, ζ, for unmelted, columnar and equiaxed regions. Optical macrograph image is shown to scale for comparison.

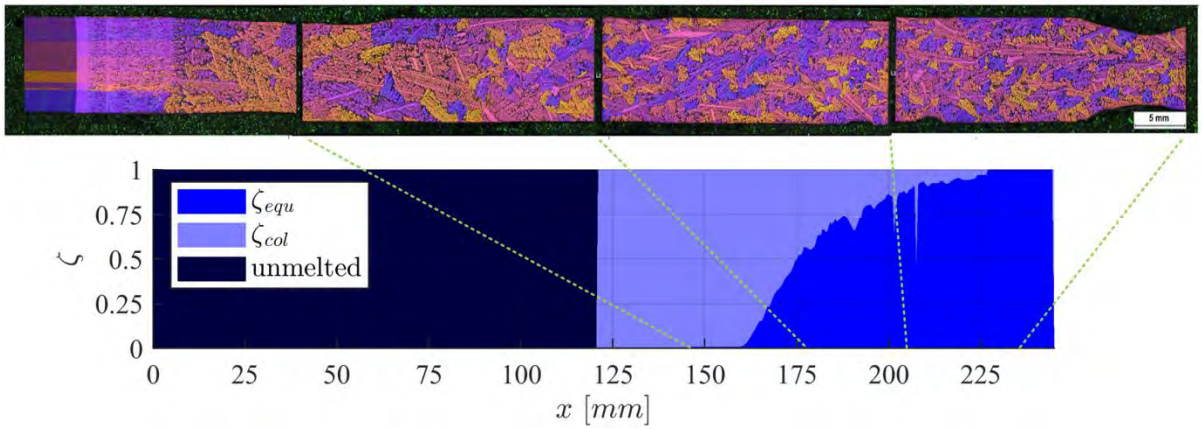

Figure 10: Final plot from the simulation for scenario GD#2 showing the volume fractions, ζ, for unmelted, columnar and equiaxed regions. Optical macrograph image is shown to scale for comparison.

In Figure 10, the morphology within the macrograph shows a progressive transition from fully columnar to fully equiaxed over the entire length of the solidified portion of the sample. The result from the C2ET model for GD#2 shows a gradual change from fully columnar to fully equiaxed. For improved clarity, Figure 11 shows the entire macrostructure for scenario GD#2 in a collage of four micrographs. The unmelted portion of the sample is clearly shown on the left of Figure 11 (a) followed by columnar dendrites shown on the right. There is axial

misalignment in the initial columnar structure due to initial growth alignment from seed and growth competition; nevertheless, it can be classified as columnar. Figure 11(b) and (c) show a region of elongated dendrites, which is representative of a misaligned elongated grain morphology, nevertheless, the grain structure shows an increased presence of smaller, equiaxed dendrites interspersed through the elongated dendrites. Figure 11(d) shows the final section of the sample, where the grain structure is more refined (i.e., with smaller equiaxed gains) than shown in Figure 11(a) and (b). Nevertheless, both equiaxed and elongated dendrites are present along the sample in all sections; hence there is a progressive CET but with an increase in equiaxed grains over elongated ones as the sample is viewed over its length from left to right.

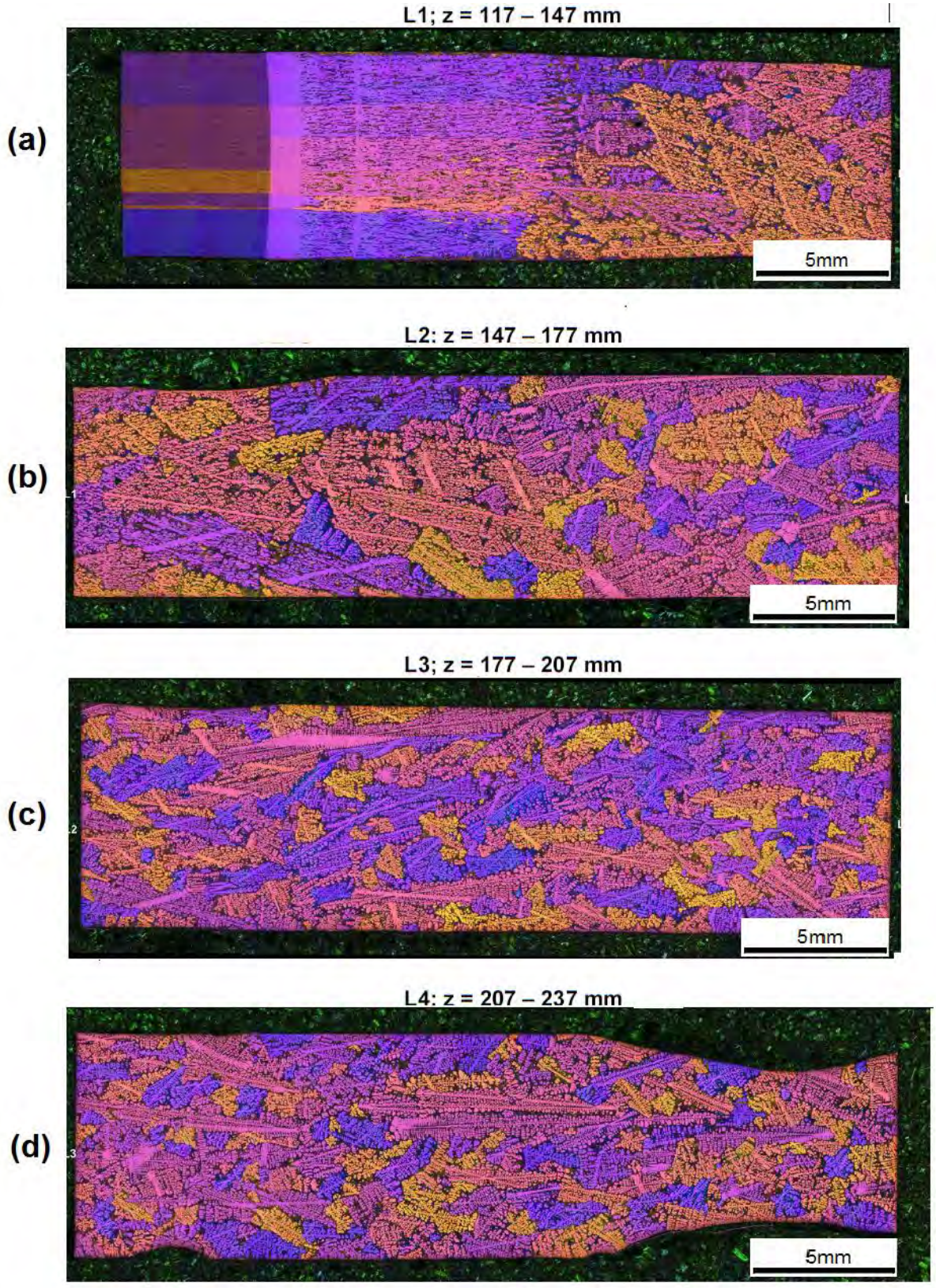

Figure 11: Microstructure image collage for scenario GD#2. Electrolytic etch under a polarising light. Representative axial positions for each micrograph are provided above each image.

5 Discussion

5.1 Comparison of the C2ET modelling outputs to the experimental findings

Numerical verification is important in any simulation exercise and results need to be confirmed as mesh independent. Each result was checked through a mesh refinement exercise and found to have converged adequately without any further refinement being necessary. Figure 5 shows the agreement achieved between the simulations and the experiments. In particular, the agreement across the solidifying temperature range between the liquidus and eutectic temperatures (618 ^{o}C and 577 ^{o}C, respectively) is good. These results show that the boundary conditions and latent heat algorithm gave realistic outputs across all scenarios for the temperature ranges on interest.

Figures 7 and 8 show the simulation results for the velocity-jump scenarios: VJ#1 and VJ#2. Each case showed a sharp CET occurring at the moment the sample temperature changed in response to the velocity step change or velocity jump imposed on the travelling furnace. The solidification front growth rates within each VJ sample increased in response to the velocity jump. Higher undercooling levels developed ahead of the columnar front. The rise in constitutional undercooling ahead of the columnar front gave the opportunity for rapid equiaxed nucleation and growth; hence, the sharp CET. The thermal response of the sample to the velocity jump happened at a sufficient rate of change for the equiaxed zone to develop fully and block the columnar dendrites. The sharp rise in ζ_{equ} in both Figures 7 and 8 corresponds well with the measured position of the CET in each case (127mm in VJ#1 and 134mm in VJ#2).

Figures 9 and 10 show the simulation results for gradient-decrease scenarios; GD#1 and GD#2. The thermal response of the sample to the change of thermal conditions in each case happened more gradually than in the VJ scenarios. This slower response led to lower equiaxed nucleation rates, so that the CET occurred in a progressive fashion in line with the rate of change of the thermal conditions. Comparisons between the macrostructure diagrams

and the model predictions show reasonable agreement to the measured start and finish positions for the CET. The macrostructure of GD#2, as shown in Figure 11, is almost completely progressive with elongated and equiaxed throughout but with an increase in the proportion of equiaxed along the sample length. The same progressive characteristic for the equiaxed fraction is captured to good effect within the simulation results of GD#2.

Equiaxed structure development solidified under moderate temperature gradients has been investigated in situ by synchrotron radiography [50]. It was shown (as discussed in [51]) that equiaxed crystals with primary arms well aligned to the heat flow direction became elongated along that preferential direction (following a Walton-Chalmers mechanism for preferential orientation selection [52]). Hence, these crystals become less equiaxed and more like columnar crystals. Other crystals observed in the radiography experiments of ref. [50] experienced sedimentation due to gravity and had rotated to find a mechanically stable orientation after impingement with the solidification front. In these cases, the orientation tended towards a V shape crystal where no arms displayed preferential orientation.
Because, in our case, the experiments were conducted in microgravity, the sedimentation and gravity-assisted rotation of crystals can be ruled out (as proven in [53]); hence it is likely that a reasonable proportion of equiaxed crystals had preferential orientation and, after impingement, became integrated as part of the progressive columnar front. The model makes no distinction between the original columnar or new elongated crystals in the composition of the columnar front behind the marker. With this aspect in mind, the progressive change from majority columnar to majority equiaxed in GD#2 is captured to good effect within the simulation.

5.2 Comparison with the analytical mechanical blocking criterion

Even though Hunt's model [7] is a steady-state model, it is useful to superimpose transient temperature information onto Hunt's diagram; thereby, allowing a quasi-steady analysis. As described earlier, the Hunt diagram consists of two curves derived from equations (1) and (2) plotted on a graph of front growth rate versus temperature gradient at the front. Growth conditions that are represented above the equiaxed line (the solid line in Figure 12) are expected to give fully equiaxed structures. Any parameters that give conditions below the columnar line (dashed line) are expected to give columnar structures. In between these two

curves, Hunt's model predicts a mixed columnar-equiaxed structure. The Hunt diagram in Figure 12 was generated using $N_o = 5 \times 10^{10}$ m^{-3} (as used in all previous scenarios) and $\Delta T_N = 2.5$ °C. The value of ΔT_N selected for the Hunt diagram is lower than the mean nucleation undercooling adapted from Liu et al. (where ΔT_μ= 4 °C). Hunt's model assumes nucleation site saturation at a single value of undercooling. Therefore, it is expected that due to the inefficiency of grain refiners, average nucleation undercooling for nucleated particles is lower than the mean undercooling for all grain refiner particles. The value of $\Delta T_N = 2.5$ °C is a reasonable approximation, as is demonstrated in other in-situ investigations [54].

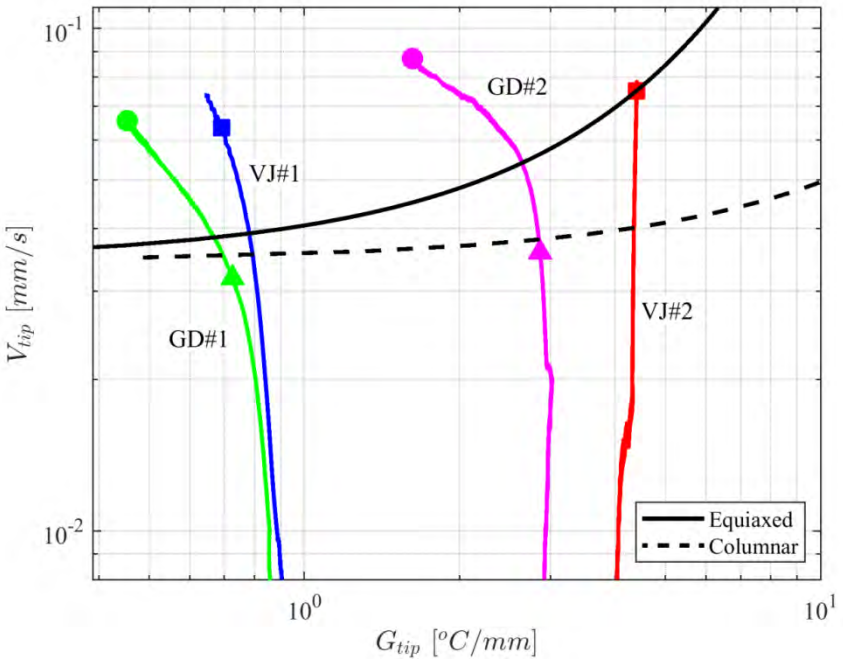

Figure 12: Growth rate, V_{tip}, versus temperature gradient, G_{tip}, at the columnar marker for all four scenarios. Square markers represent sharp CETs. Triangular and circular markers represent the start and end of progressive CETs, respectively. Also shown for reference are Hunt lines for fully equiaxed (solid line) and fully columnar (broken line) using parameters N_o = 5×10^{10} m^{-3} and ΔT_N = 2.5 °C.

Since the columnar marker in the C2ET is tracked, the temperature gradient and growth rate are provided at each time step in each solution. This pairing of information has been superimposed onto the Hunt diagram to give a locus of points for each experimental scenario. The intention for each experiment was to start with thermal conditions within the fully columnar region (below the dashed line) and then to progress into the equiaxed region (above

the equiaxed line). Samples processed within the first flight batch (VJ#1 and GD#1) were selected with initial conditions with relatively low temperature gradients around 0.8 to 0.9 ºC/mm. Samples processed within the second flight batch (VJ#2 and GD#2) were selected to have initial gradients (3 to 4 ºC/mm) that were an order of magnitude higher than the first batch. The temperature gradients are shown to reduce throughout each simulation. The gradient reductions for the GD cases are more obvious. Temperature gradients are reasonably well maintained at their initial levels for the VJ cases. In all cases, the growth rates, v_{tip}, are predicted to rise to approximately by an order of magnitude higher in all experimental cases.

The markers on the locus lines show the predicted start-finish positions for the CETs that have been shown to correlate well with the observed microstructures. Although the Hunt lines are based on estimated nucleation information, they are useful in providing qualitative judgements around the nature of the transitions. At the lower temperature gradients, the Hunt diagram (with estimated data) predicts that the transition from fully columnar to fully equiaxed ought to be quite narrow. The Hunt theory under the assumed conditions would support the case for a sharp CET at low temperatures gradients; however, this was not the case for GD#1 which had a progressive CET. Similarly, at the higher temperature gradients of flight batch two (VJ#2 and GD#2) the Hunt diagram shows a larger gap between the fully columnar and equiaxed lines. Given that cooling rates (estimated by the product $G_{tip}v_{tip}$) are higher, it would still be expected that progressive CET should be favoured at higher gradients due to the divergence of the Hunt lines. Scenario VJ#2 clearly showed a sharp CET without evidence of mixed zone occurring. This result could be explained by the VJ#2 having the fastest cooling rates and a rapid transition along its locus of points shown in Figure 12.

The current exercise demonstrates the difficulty in establishing a single set of nucleation parameters for the Hunt model that agrees well with all of the CET datasets. In contrast to this, the C2ET, which gave a thermally transient solution for each case, used the same nucleation parameters in all cases and gave good agreement to measured CET positions for all four experimental datasets.

6 Conclusion

Four microgravity experiments showed examples of sharp and progressive columnar to equiaxed transitions under different thermal processing parameters. The presence of the progressive transition, in particular, established the need to focus on the mixed columnar-equiaxed region. In literature, the Hunt blocking fraction of $\phi = 0.49$ (based on the extended volume fraction $\phi_E = 0.66$) was provided to predict the transition from a mixed structure to a fully equiaxed structure. On the other hand, the extended volume fraction of $\phi_E = 0.0066$ was provided to predict the transition from a fully columnar region to a mixed columnar-equiaxed region. Through this study, the Hunt blocking fractions have been directly tested against thermally transient simulation results and have been shown to lack the robustness to give universal agreement across all experimental cases investigated.

Hence, a model of Columnar to Equiaxed Transition has been proposed and validated that allows columnar and equiaxed regions to grow concurrently and competitively. The columnar region is modelled using a front tracking approach based on the principles of Browne and Hunt [11] within the BFFTM model [39] and the equiaxed model follows the Nucleation Progenitor Function approach [43].

This approach known as the Concurrent Columnar to Equiaxed Transition (C2ET) model was able to predict thermal profiles with good agreement. In addition, it modelled the complete transition from fully columnar to fully equiaxed regions with a progressive columnar-to-equiaxed region. Both the sharp and progressive transitions (as observed in the experimental cases) have been modelled successfully.

7 Acknowledgments

This work was performed as part of the ESA funded CETSOL-5 Microgravity Application Programme as part of the ELIPS-4 programme [contract number AO-99-117, CETSOL]. Authors RM and SMF acknowledge the financial support of ESA PRODEX [contract number 4000107132] as managed by Irish Space Delegation at Enterprise Ireland. Authors LZ and GZ acknowledge financial support of the European Space Agency under the CETSOL ESA MAP contract number AO-99-117 and of the German BMWi/DLR under FKZ 50WM1743.

Authors Y.L, HN-T and NM-N acknowledge financial support of the European Space Agency under the CETSOL ESA MAP contract number AO-99-117 and the French National Space Agency (CNES).

8 Data availability

The raw/processed data required to reproduce these findings cannot be shared at this time due to technical or time limitations.

9 References

[1] J.A. Spittle, Columnar to equiaxed grain transition in as solidified alloys, Int. Mater. Rev. 51 (2006) 247–269. doi:10.1179/174328006X102493.

[2] M. Haines, A. Plotkowski, C.L. Frederick, E.J. Schwalbach, S.S. Babu, A sensitivity analysis of the columnar-to-equiaxed transition for Ni-based superalloys in electron beam additive manufacturing, Comput. Mater. Sci. 155 (2018) 340–349. doi:10.1016/j.commatsci.2018.08.064.

[3] F. Versnyder, M. Shank, The development of columnar grain and single crystal high temperature materials through directional solidification, Mater. Sci. Eng. 6 (1970) 214–247.

[4] E.O. Hall, The deformation and ageing of mild steel: III Discussion of results, Proc. Phys. Soc. Sect. B. 64 (1951) 747–753. doi:10.1088/0370-1301/64/9/303.

[5] N.J. Petch, The cleavage strength of polycrystals, J. Iron Steel Inst. 174 (1953) 25–28.

[6] W. Wolczynski, A.A. Ivanowa, P. Kwapisinski, Mathematical predictions of brass/steel ingot structures, Sci. Journals Marit. Univ. Szczecin-Zeszyty Nauk. Akad. Morskiej W Szczecinie. 56 (2018) 47–54. doi:10.17402/313.

[7] J.D. Hunt, Steady State Columnar Equiaxed Growth of Dendrites and Eutectic, Mater. Sci. Eng. 65 (1984) 75–83.

[8] M.A. Martorano, C. Beckermann, C.A. Gandin, A solutal interaction mechanism for the columnar-to-equiaxed transition in alloy solidification, Metall. Mater. Trans. A Phys. Metall. Mater. Sci. 34 A (2003) 1657–1674. doi:10.1007/s11661-003-0311-x.

[9] H.B. Dong, P.D. Lee, Simulation of the columnar-to-equiaxed transition in directionally solidified Al-Cu alloys, Acta Mater. 53 (2005) 659–668.

doi:10.1016/j.actamat.2004.10.019.

[10] A. Badillo, C. Beckermann, Phase-field simulation of the columnar-to-equiaxed transition in alloy solidification, Acta Mater. 54 (2006) 2015–2026. doi:10.1016/j.actamat.2005.12.025.

[11] D.J. Browne, J.D. Hunt, A Fixed Grid Front-Tracking Model of the Growth of a Columnar Front and an Equiaxed Grain during Solidification of an Alloy, Numer. Heat Transf. Part B Fundam. 45 (2004) 395–419. doi:10.1080/10407790490430606.

[12] S. McFadden, D.J. Browne, A front-tracking model to predict solidification macrostructures and columnar to equiaxed transitions in alloy castings, Appl. Math. Model. 33 (2009) 1397–1416.

[13] W.U. Mirihanage, D.J. Browne, G. Zimmermann, L. Sturz, Simulation of international space station microgravity directional solidification experiments on columnar-to-equiaxed transition, Acta Mater. (2012). doi:10.1016/j.actamat.2012.08.015.

[14] W.U. Mirihanage, H. Dai, H. Dong, D.J. Browne, Computational modeling of columnar to equiaxed transition in alloy solidification, Adv. Eng. Mater. 15 (2013) 216–229. doi:10.1002/adem.201200220.

[15] D. Tourret, A. Karma, Three-dimensional dendritic needle network model for alloy solidification, Acta Mater. 120 (2016) 240–254. doi:10.1016/j.actamat.2016.08.041.

[16] P.A. Geslin, C.H. Chen, A.M. Tabrizi, A. Karma, Dendritic needle network modeling of the Columnar-to-Equiaxed transition. Part I: two dimensional formulation and comparison with theory, Acta Mater. 202 (2021) 42–54. doi:10.1016/j.actamat.2020.10.009.

[17] C.H. Chen, A.M. Tabrizi, P.A. Geslin, A. Karma, Dendritic needle network modeling of the Columnar-to-Equiaxed Transition. Part II: three dimensional formulation, implementation and comparison with experiments, Acta Mater. 202 (2021) 463–477. doi:10.1016/j.actamat.2020.10.012.

[18] D.R. Liu, N. Mangelinck-Noël, C.A. Gandin, G. Zimmermann, L. Sturz, H. Nguyen-Thi, et al., Structures in directionally solidified Al-7 wt.% Si alloys: Benchmark experiments under microgravity, Acta Mater. 64 (2014) 253–265. doi:10.1016/j.actamat.2013.10.038.

[19] Y.Z. Li, N. Mangelinck-Noël, G. Zimmermann, L. Sturz, H. Nguyen-Thi, Effect of solidification conditions and surface pores on the microstructure and columnar-to-

equiaxed transition in solidification under microgravity, J. Alloys Compd. 749 (2018) 344–354. doi:10.1016/j.jallcom.2018.03.300.

[20] Y.Z. Li, N. Mangelinck-Noël, G. Zimmermann, L. Sturz, H. Nguyen-Thi, Comparative study of directional solidification of Al-7 wt% Si alloys in Space and on Earth: Effects of gravity on dendrite growth and Columnar-to-equiaxed transition, J. Cryst. Growth. 513 (2019) 20–29. doi:10.1016/j.jcrysgro.2019.02.050.

[21] Y.Z. Li, N. Mangelinck-Noël, G. Zimmermann, L. Sturz, H. Nguyen-Thi, Modification of the microstructure by rotating magnetic field during the solidification of Al-7 wt.% Si alloy under microgravity, J. Alloys Compd. 836 (2020). doi:10.1016/j.jallcom.2020.155458.

[22] M. Gäumann, R. Trivedi, W. Kurz, Nucleation ahead of the advancing interface in directional solidification, Mater. Sci. Eng. A. 226–228 (1997) 763–769. doi:10.1016/s0921-5093(97)80081-0.

[23] W. Kurz, B. Giovanola, R. Trivedi, Theory of microstructural development during rapid solidification, Acta Metall. 34 (1986) 823–830. doi:10.1016/0001-6160(86)90056-8.

[24] S.C. Flood, J.D. Hunt, Columnar and equiaxed growth. II. Equiaxed growth ahead of a columnar front, J. Cryst. Growth. 82 (1987) 552–560. doi:10.1016/0022-0248(87)90347-2.

[25] S.C. Flood, J.D. Hunt, Columnar and equiaxed growth. I. A model of a columnar front with a temperature dependent velocity, J. Cryst. Growth. 82 (1987) 543–551. doi:10.1016/0022-0248(87)90346-0.

[26] V.B. Biscuola, M.A. Martorano, Mechanical blocking mechanism for the columnar to equiaxed transition, Metall. Mater. Trans. A Phys. Metall. Mater. Sci. 39 (2008) 2885–2895. doi:10.1007/s11661-008-9643-x.

[27] S. Sachi, M. Založnik, H. Combeau, C.A. Gandin, M. Gennesson, J. Demurger, et al., Analysis of columnar-to-equiaxed transition experiment in lab scale steel casting by a multiphase model, IOP Conf. Ser. Mater. Sci. Eng. 529 (2019). doi:10.1088/1757-899X/529/1/012039.

[28] D.A. Pineda, M.A. Martorano, Columnar to equiaxed transition in directional solidification of inoculated melts, Acta Mater. 61 (2013) 1785–1797. doi:10.1016/j.actamat.2012.12.002.

[29] W. Mirihanage, S. McFadden, D.J. Browne, Macroscopic Model for Predicting Columnar to Equiaxed Transitions Using Columnar Front Tracking and Average Equiaxed Growth, Mater. Sci. Forum. (2010). doi:10.4028/www.scientific.net/MSF.649.355.

[30] M. Wu, A. Ludwig, A Three-Phase Model for Mixed Columnar-Equiaxed Solidification, Metall. Mater. Trans. A. 37A (2006) 1613–1631. doi:10.1007/s11661-006-0104-0.

[31] M. Wu, A. Fjeld, A. Ludwig, Modelling mixed columnar-equiaxed solidification with melt convection and grain sedimentation - Part I: Model description, Comput. Mater. Sci. 50 (2010) 32–42. doi:10.1016/j.commatsci.2010.07.005.

[32] M. Wu, A. Ludwig, A. Fjeld, Modelling mixed columnar-equiaxed solidification with melt convection and grain sedimentation - Part II: Illustrative modelling results and parameter studies, Comput. Mater. Sci. 50 (2010) 43–58. doi:10.1016/j.commatsci.2010.07.006.

[33] M. Wu, A. Ludwig, A. Kharicha, Volume-averaged modeling of multiphase flow phenomena during alloy solidification, Metals (Basel). 9 (2019). doi:10.3390/met9020229.

[34] W. Wołczyński, A.A. Ivanova, P. Kwapisiński, On consonance between a mathematical method for the CET prediction and constrained / unconstrained solidification, Procedia Manuf. 30 (2019) 459–466. doi:10.1016/j.promfg.2019.02.065.

[35] F. Ngomesse, G. Reinhart, H. Soltani, G. Zimmermann, D.J. Browne, W. Sillekens, et al., In situ investigation of the Columnar-to-Equiaxed Transition during directional solidification of Al–20wt.%Cu alloys on Earth and in microgravity, Acta Mater. 221 (2021) 117401. doi:10.1016/j.actamat.2021.117401.

[36] D.R. Liu, N. Mangelinck-Noël, C.A. Gandin, G. Zimmermann, L. Sturz, H. Nguyen-Thi, et al., Simulation of directional solidification of refined Al-7 wt.%Si alloys - Comparison with benchmark microgravity experiments, Acta Mater. 93 (2015) 24–37. doi:10.1016/j.actamat.2015.03.058.

[37] G. Zimmermann, L. Sturz, H. Nguyen-Thi, N. Mangelinck-Noel, Y.Z. Li, C.A. Gandin, et al., Columnar and Equiaxed Solidification of Al-7 wt.% Si Alloys in Reduced Gravity in the Framework of the CETSOL Project, JOM. 69 (2017) 1269–1279. doi:10.1007/s11837-017-2397-4.

[38] S. Battaglioli, S. McFadden, A.J. Robinson, Numerical simulation of Bridgman solidification of binary alloys, Int. J. Heat Mass Transf. 104 (2017) 199–211. doi:10.1016/j.ijheatmasstransfer.2016.08.030.

[39] R.P. Mooney, S. McFadden, M. Rebow, D.J. Browne, A Front Tracking Model for Transient Solidification of Al–7wt%Si in a Bridgman Furnace, Trans. Indian Inst. Met. 65 (2012) 527–530. doi:10.1007/s12666-012-0201-2.

[40] R.P. Mooney, S. McFadden, Z. Gabalcová, J. Lapin, An experimental-numerical method for estimating heat transfer in a Bridgman furnace, Appl. Therm. Eng. 67 (2014) 61–71. doi:10.1016/j.applthermaleng.2014.02.048.

[41] R.P. Mooney, S. McFadden, Order verification of a Bridgman furnace front tracking model in steady state, Simul. Model. Pract. Theory. 48 (2014) 24–34. doi:10.1016/j.simpat.2014.07.005.

[42] R.P. Mooney, U. Hecht, Z. Gabalcová, J. Lapin, S. McFadden, Directional solidification of a TiAl alloy by combined Bridgman and power-down technique, Kov. Mater. 53 (2015). doi:10.4149/km-2015-3-187.

[43] S. McFadden, R.P. Mooney, L. Sturz, G. Zimmermann, A Nucleation Progenitor Function approach to polycrystalline equiaxed solidification modelling with application to a microgravity transparent alloy experiment observed in-situ, Acta Mater. 148 (2018) 289–299. doi:10.1016/j.actamat.2018.02.012.

[44] A.N. Kolmogorov, No Title, Bull. Acad. Sci. URSS (Sci. Math. Nat.). 3 (1937) 355.

[45] M. Avrami, Kinetics of Phase Change. I General Theory, J. Chem. Phys. 7 (1939) 1103. doi:10.1063/1.1750380.

[46] M. Avrami, Kinetics of Phase Change. II Transformation-Time Relations for Random Distribution of Nuclei, J. Chem. Phys. 8 (1940) 212. doi:10.1063/1.1750631.

[47] M. Tomellini, M. Fanfoni, Why phantom nuclei must be considered in the Johnson-Mehl-Avrami-Kolmogoroff kinetics, Phys. Rev. B. 55 (1997) 14071–14073. doi:10.1103/PhysRevB.55.14071.

[48] S. McFadden, P.L. Schaffer, R.H. Mathiesen, D.J. Browne, Analysis of an Equiaxed Dendrite Growth Model with Comparisons to *In-Situ* Results of Equiaxed Dendritic Growth in an Al-Ge Alloy, Mater. Sci. Forum. 654–656 (2010) 1359–1362. doi:10.4028/www.scientific.net/MSF.654-656.1359.

[49] S. McFadden, D.J. Browne, C.A. Gandin, A comparison of columnar-to-equiaxed

transition prediction methods using simulation of the growing columnar front, Metall. Mater. Trans. A Phys. Metall. Mater. Sci. 40 (2009) 662–672. doi:10.1007/s11661-008-9708-x.

[50] G. Reinhart, N. Mangelinck-Noël, H. Nguyen-Thi, T. Schenk, J. Gastaldi, B. Billia, et al., Investigation of columnar–equiaxed transition and equiaxed growth of aluminium based alloys by X-ray radiography, Mater. Sci. Eng. A. 413–414 (2005) 384–388. doi:10.1016/j.msea.2005.08.197.

[51] J.A. Dantzig, M. Rappaz, Solidification, 2nd ed., EPFL press (CRC Press), 2016.

[52] D. Walton, B. Chalmers, The Origin of the Preferred Orientation in the Columnar Zone of Ingots, Trans. Metall. Soc. AIME, Vol. 215. 215 (1959) 3–13.

[53] A.G. Murphy, R.H. Mathiesen, Y. Houltz, J. Li, C. Lockowandt, K. Henriksson, et al., Direct observation of spatially isothermal equiaxed solidification of an Al–Cu alloy in microgravity on board the MASER 13 sounding rocket, J. Cryst. Growth. 454 (2016) 96–104. doi:10.1016/j.jcrysgro.2016.08.054.

[54] N. Mangelinck-Noël, J.E. Spinelli, C.-A. Gandin, G. Reinhart, H. Nguyen-Thi, B. Billia, A method to determine the active particle nucleation undercooling distribution in a refined alloy, IOP Conf. Ser. Mater. Sci. Eng. 27 (2011) 012090. doi:10.1088/1757-899X/27/1/012090.